1 # Hyperspectral reflectance spectra of floating matters derived from

2 # HICO observations

3 Chuanmin Hu

4 College of Marine Science, University of South Florida, St. Petersburg, Florida, 33701, USA

5 *Correspondence to:* Chuanmin Hu (huc@usf.edu)

6 **Abstract**

7 Using data collected by the Hyperspectral Imager for the Coastal Ocean (HICO) on the International Space Station

8 between 2010 – 2014, hyperspectral reflectance of various floating matters in global oceans and lakes are derived for

9 the spectral range of 400 – 800 nm. Specifically, the entire HICO archive of 9,411 scenes is first visually inspected to

10 identify suspicious image slicks. Then, a nearest-neighboring atmospheric correction is used to derive surface

11 reflectance of slick pixels. Finally, a spectral unmixing scheme is used to derive the reflectance spectra of floating

12 matters. Analysis of the spectral shapes of these various floating matters (macroalgae, microalgae, organic particles,

13 whitecaps) through the use of a Spectral Angle Mapper (SAM) index indicates that they can mostly be distinguished

14 from each other without the need of ancillary information. Such reflectance spectra from the consistent 90-m resolution

15 HICO observations are expected to provide spectral endmembers to differentiate and quantify the various floating

16 matters from existing multi-band satellite sensors and future hyperspectral satellite missions such as NASA's Plankton,

17 Aerosol, Cloud, and ocean Ecosystem (PACE) mission and Surface Biology and Geology (SBG) mission.

18

19 **Keywords:** Remote sensing, hyperspectral, HICO, OCI, PACE, SBG, floating matters, *Ulva, Sargassum, Noctiluca,*

20 *Trichodesmium, Microcystis,* brine shrimp, oil slicks, whitecaps, marine debris.

21 ## 1. Introduction

22 Since the debut of the first proof-of-concept Coastal Zone Color Scanner (CZCS, 1978 – 1986), satellite ocean color

23 missions have evolved from the original goal of mapping phytoplankton biomass and primary production to many

24 other applications. Because of improved spectral resolution and instrument sensitivity, mapping various floating

25 matters also becomes possible (IOCCG, 2014). These floating matters range from living to non-living, including

26 *Sargassum* macroalgae, *Ulva* macroalgae, cyanobacterium *Microcystis*, cyanobacterium *Trichodesmium*,

27 dinoflagellate *Noctiluca*, aquatic plants, brine shrimp cysts, oil slicks, pumice rafts, marine debris, among others (Qi

28 et al., 2020).

29 Currently, mapping floating matters using optical remote sensing requires the detection of a spatial anomaly using the

30 near-infrared (NIR) bands, and then discrimination of the anomaly by comparing its spectral characteristics with

31 known spectra of floating matters (Qi et al., 2020), or by using ancillary information (e.g., in certain regions a spatial

32 anomaly can only be caused by a certain type of floating algae). Spectral discrimination requires the knowledge of

33   spectral signitures of various floating matters. However, despite scattered laboratory or field measurements of certain

34   types of floating matters, hyperspectral data of these floating matters are mostly unavailable. Although medium-

35   resolution (300-m) sensors such as the Ocean and Land Colour Imager (OLCI) has been used to show spectral

36   variations of floating matters (Qi et al., 2020), the data are not hyperspectral, therefore certain spectral features may

37   have been missed.

38   Data collected by the Hyperspectral Imager for the Coastal Ocean (HICO) on the International Space Station may fill

39   this gap. HICO has 128 bands covering a spectral range of 353 – 1080 nm. From its entire mission of 2010 – 2014, a

40   total of 9,411 scenes have been collected at a spatial resolution of about 90 m, each containing about 512×2000

41   pixels. On average, only 6 scenes were collected per day around the globe, mostly over land and coastal waters.

42   However, because of its stable calibration (Ibrahim et al., 2018) and relatively high signal-to-noise ratios (Hu et al.,

43   2012), deriving hyperspectral surface reflectance of water targets should be feasible.

44   The primary objective of this paper is to derive HICO-based hyperspectral reflectance of various floating matters.

45   From such derived spectra, a secondary objective is to analyze whether they can be differentiated spectrally. Similar

46   to the compiled hyperspectral dataset for inherent and apparent optical properties to support future hyperspectral

47   missions such as NASA's Plankton, Aerosol, Cloud, and ocean Ecosystem (PACE) mission (Casey et al., 2020), such

48   a dataset for floating matters is expected to help develop or improve algorithms for the PACE mission as well as for

49   the hyperspectral Surface Biology and Geology mission currently being planned by NASA (Cawse-Nicholson et al.,

50   2021).

51   **2. Data and Methods**

52   HICO Level-1B (calibrated radiance) data were obtained from the NASA Goddard Space Flight Center

53   (https://oceancolor.gsfc.nasa.gov). All 9,411 scenes were downloaded, and the following 4 steps were used to derive

54   spectral reflectance of various floating matters.

55   Step 1 is to generate quick look Red-Green-Blue (RGB) and False-color RGB (FRGB) images with Rayleigh corrected

56   reflectance (R_{rc}, dimensionless) in three HICO bands using the same methods as in Qi et al. (2020). In the FRGB

57   images, a near-infrared (NIR) band is used to represent the green channel, thus making floating matters often appear

58   greenish due to their elevated NIR reflectance. Here, R_{rc} was generated using the NASA software SeaDAS (version

59   7.5). Mathematically, it is derived as

60    $$R_{rc} = (R_t - R_r)/(t\, t_o\, t_{O2}\, t_{H2O}),$$

61    $$R_t = \pi\, L_t^* / F_o \cos(\theta_o),$$

62    $$R_r = \pi\, L_r / F_o \cos(\theta_o), \tag{1}$$

63   where L_t^* is the at-sensor total radiance after vicarious calibration and adjustment of two-way gaseous absorption (e.g.,

64   Ozone), L_r is at-sensor radiance due to Rayleigh scattering, F_o is the extraterrestrial solar irradiance, θ_o is the solar

65   zenith angle, t is the diffuse transmittance from the image pixel to the satellite, t_o is the diffuse transmittance from the

66   sun to the image pixel, t_{O2} and t_{H2O} are the two-way transmittance due to absorption by atmospheric O_2 and H_2O,

67   respectively. For simplicity, the wavelength dependency is omitted here.

68   Step 2 is to determine image slicks through visual inspection of both RGB and FRGB images. Fig. 1a shows an FRGB

69   image captured in the central western Atlantic, where an elongated greenish slick is identified.

70   Step 3 is to derive surface reflectance (R, dimensionless) of the slick pixels (i.e., those containing floating matters)

71   *and* nearby water pixels. While the latter is straightforward because R at each pixel is a standard output of the SeaDAS

72   software, the former is problematic because standard atmospheric correction in SeaDAS fails over floating matters

73   due to their elevated NIR reflectance. Such elevated NIR reflectance violates the atmospheric correction assumptions

74   (i.e., negligible reflectance in the NIR, or fixed relationships between the red and NIR wavelengths) for slick pixels.

75   Therefore, a nearest-neighbor atmospheric correction (Hu et al., 2000) was used to estimate R of the slick pixels.

76   Specifically, from the SeaDAS output of R_{rs}, we have

77    $$R = \pi\, R_{rs} = (R_t - R_r - R_a)/(t\, t_o\, t_{O2}\, t_{H2O}), \qquad (2)$$

78   where R_{rs} is the surface remote sensing reflectance (sr^{-1}), R_a is the at-sensor aerosol reflectance (and reflectance due

79   to aerosol-molecule interactions as well as due to sun glint and whitecaps). The difference between R and R_{rc} in Eqs.

80   (2) and (1), respectively, is the removal of R_a in (2). Estimation of R_a at each pixel represents the "core" of any

81   atmospheric correction scheme. The SeaDAS estimation of R_a is valid over water pixels, but not valid over the slick

82   pixels. Therefore, R_a over water pixels was used as a surrogate to represent R_a over the nearby slick pixels, from which

83   R over slick pixels was derived. This is why such an approach is called "nearest-neighbor" atmospheric correction

84   (Hu et al., 2000). In this context, the slick pixel is called "target", and the nearby water pixel is called "reference".

85   Their surface reflectance are called R^T and R^R, respectively. Fig. 1b shows examples of R^T and R^R.

86
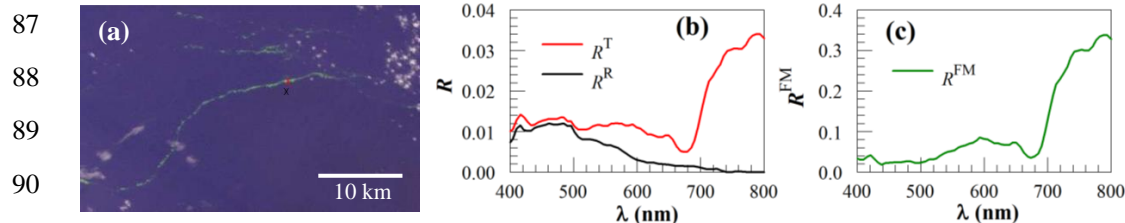
87
88
89
90
91

92   **Figure 1. Demonstration of how surface reflectance of floating matter (R^{FM}) is derived. (a) FRGB image on 1 July 2012**

93   **showing several greenish image slicks in the Amazon River plume. The image covers a region of about 40 km × 24 km, with**

94   **the "Target" (6.65914ºN, 51.2395ºW) and "Reference" (6.64847ºN, 51.2411ºW) pixels marked with a red "×" and a black**

95   **"×", respectively. (b) Their corresponding R^T and R^R, with the latter derived from SeaDAS and the former derived from a**

96   **nearest-neighbor atmospheric correction. (c) R^{FM} derived from R^T and R^R using Eq. (4), with χ being estimated to be 10%.**

97

98   The final step, Step 4, is to perform spectral unmixing of R^T. This is because floating matters often cover only a small
99   portion a pixel (Hu, 2021a). In this step, the derived R^T from Step 3 is assumed to be a linear mixture of two
100 endmembers: floating matter (R^{FM}) and water (R^W):

101              $$R^T = \chi R^{FM} + (1 - \chi)R^W = \chi R^{FM} + (1 - \chi)R^R \qquad (3)$$

102 Here, χ is the subpixel portion of floating matter which can vary between 0.0% and 100%, R^W is assumed to be R^R.
103 Then, the final product, R^{FM}, is derived as

104              $$R^{FM} = R^R + (R^T - R^R)/\chi \qquad (4)$$

105 In the right-hand side of Eq. (4), the only unknown is χ. In practice, assuming R^{FM} at 750 nm $\approx$ 0.3 as revealed by
106 independent measurements of floating macroalgae (Hu, L. et al., 2017; Wang et al., 2018), χ is estimated through
107 linear unmixing as

108              $$\chi = [R^T(754) - R^R(754)]/[0.3 - R^R(754)] \qquad (5)$$

109 Here, with $R^T(754)$ varying between $R^R(754)$ and 0.3, χ ranges between 0.0% and 100%. Plugging this mixing ratio
110 into Eq. (4) will derive R^{FM}. Fig. 1c shows the example of how R^{FM} is derived from R^T and R^R of Fig. 1b once they are
111 known from Step 3, with χ being estimated to be 10%.

112 Once R^{FM} is derived, a spectral angle mapper index (SAM, Kruse et al., 1993) was used to determine whether different
113 floating matters were spectrally different. SAM was used because it is based on spectral shape only. SAM is the angle
114 between two spectral vectors, defined as (Kruse et al., 1993):

115              $$\text{SAM (degrees)} = \cos^{-1}[(\sum x_i y_i) / (\sqrt{\sum x_i^2} \sqrt{\sum y_i^2})]. \qquad (6)$$

116 Here, x and y represent two spectral vectors with the ith band from 1 to N. An SAM of 0° indicates identical spectral
117 shapes between x and y regardless of their difference in magnitudes, while an SAM of 90° indicates completely
118 different spectral shapes. An SAM of < 5° indicates that the two spectra are very similar (Garaba and Dierssen, 2018).

119 **3. Results: HICO reflectance spectra of floating matters**

120 The approach above was applied to the visually identified image slicks to derive $R^{FM}(\lambda)$. These include: 1) *Sargassum*
121 *fluitans/natans* in the Atlantic (including the Caribbean Sea and Gulf of Mexico), 2) *Ulva* in the western Yellow Sea
122 (near Qingdao, China), 3) *Kelp* in South Atlantic, 4) *Trichodesmium* around Australia, in the Gulf of Mexico and
123 Persian Gulf, in the South Atlantic Bight, Bay of Bengal, near Hawaii and Pagan Island (middle Pacific), 5)
124 Cyanobacteria of *Microcystis* in Taihu Lake, Lake Woods, and Lake of Victoria, 6) Red *Noctiluca scintillas* (RNS) in
125 the East China Sea, and coastal waters off Japan, 7) Brine shrimp cysts in the Great Salt Lake, 8) Oil slicks in the Gulf
126 of Mexico, 9) Whitecaps (foam) in the Arabian Sea, Caspian Sea, and Bohai Sea, 10) Ice in Lake Baykal, 11) some
127 unknown algae features. For convenience, they are grouped into 4 figures: Fig. 2 for macroalgae (*Sargassum*, *Ulva*,
128 and kelp), Fig. 3 for microalgae (*Trichodesmium*, *Microcystis*, red *Noctiluca scintillas* or *RNS*), Fig. 4 for organic
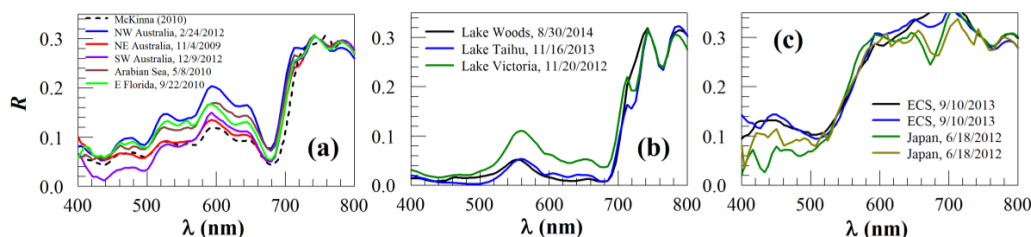129 particles and ocean/lake bubbles, and Fig. 5 for unknown algae scums.

130

131
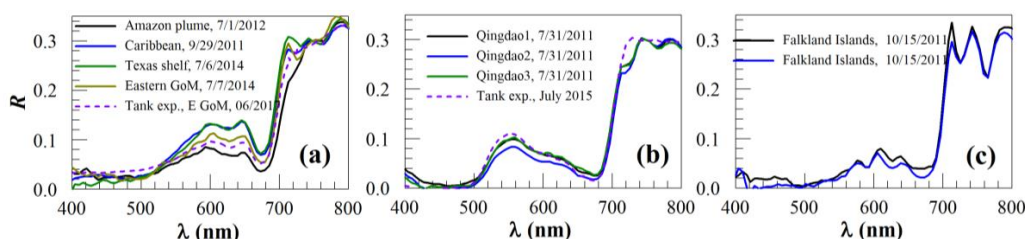
Figure 2: Surface reflectance (R, dimensionless) of macroalgae: (a) pelagic *Sargassum*, (b) *Ulva prolifera*, (c) kelp. The dashed lines in (a) and (b) denote R from water tank experiments of Wang et al. (2018) and Hu, L. et al. (2017), respectively.
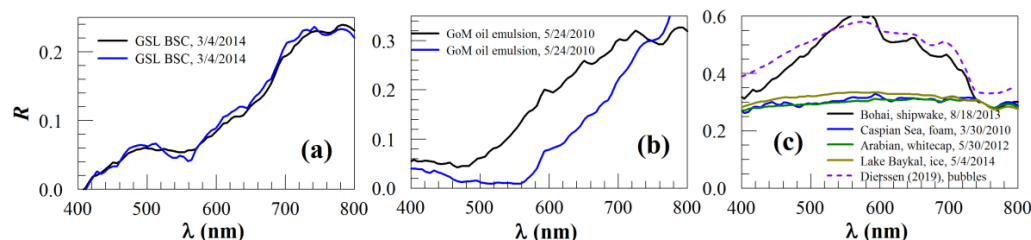
134

135

136

137

Figure 3. Surface reflectance (R, dimensionless) of floating scums of microalgae: (a) *Trichodesmium*, (b) *Microcystis*, (c) red *Noctiluca* near Yangtze River of the East China Sea and in Sagami Bay of Japan. The dashed line in (a) denote field measured R by McKinna (2010).

141

142

143

144

145

Figure 4: Surface reflectance (R, dimensionless) of various floating materials: (a) Brine shrimp cysts in the Great Salt Lake (GSL), (b) emulsified oil from the Deepwater Horizon oil spill, and (c) shipwake, seafoam, whitecap and ice. The dashed line in (c) denotes submersed bubbles measured by Dierssen (2019), which is similar to the shipwake spectrum. Note the similarity among other spectra.

Earth System
Science
Data

Open Access

Discussions

149
150
151
152
153
154
155
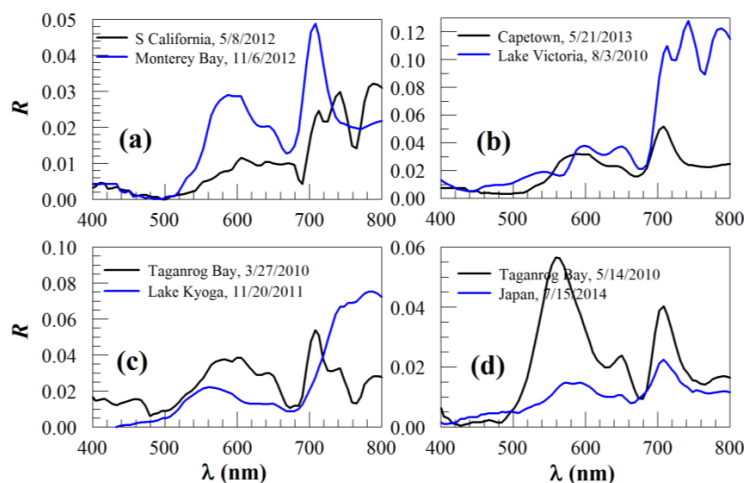156
157
158
159
160

Figure 5: Surface reflectance (*R*, dimensionless) of known and unknown algae scums. (a) Blooms off southern California and in Monterey Bay that are thought to be *Lingulodinium polyedrum* (Cetinic, 2009) and *Akashiwo sanguinea* (Jessup et al., 2009), respectively. (b) Blooms of unknown types of algae off Cape Town (South Africa) and in Lake Victoria, both likely to be dinoflagellates. Note the different spectra shape of the Lake Victoria bloom as compared with the cyanobacterial bloom in the same lake (Fig. 3b). (c) Blooms of unknown types of algae in Taganrog Bay and Lake Kyoga. (d). Blooms of unknown types of algae in Taganrog Bay (note the difference from Fig. 5c) and in Japan coastal waters.

4. Discussion

4.1. Uncertainties in the derived RFM

There are several assumptions used in the nearest-neighbor atmospheric correction and spectral unmixing (Eq. 4). Violations of these assumptions will cause errors in the derived R^{FM} spectra. For example, if the atmosphere over the floating matter pixel is different from over the nearby water, the nearest-neighbor atmospheric correction may not be applicable. In practice, however, because the target and reference pixels are very close (< 1 km), such a violation is unlikely. In Step 4, the water within the FM-containing pixel is assumed to be the same as the nearby water. Because of the close proximity of the two pixels, this assumption should be valid for most cases unless the FM-containing pixel is at an ocean front where different water masses converge. The departure of $R^{FM}(754)$ from the assumed 0.3 will also lead to errors in the estimated χ (and therefore R^{FM}). However, as long as R^{W} (i.e., R^{R}) in Eqs. (4) & (5) is $<< R^{FM}$, the shape of R^{FM} is still retained, although the magnitude departs from the "truth" in proportional to the departure of $R^{FM}(754)$ from 0.3. Indeed, the condition of $R^{W} << R^{FM}$ can be satisfied for λ > 600 nm for most floating matters unless the water is extremely turbid. Even for turbid waters, for certain floating matters where R^{FM} is elevated at λ > 530 nm (e.g., red *Noctiluca*, brine shrimp cysts, ice), the shape of the derived R^{FM} should still be valid for λ > 530 nm. Indeed,

181   when R^W is $<< R^{FM}$, even a simple subtraction of R_{rc} or TOA radiance between the target pixel and reference pixel, as

182   demonstrated in Gower et al. (2006), may retain the spectral shapes of floating matters.

183   Another uncertainty source can come from the assumption of linear mixing between floating matters and water (Eq.

184   (3)). For macroalgae, the linear mixing up to the reflectane saturation level has been shown in laboratory experiments

185   (Hu. L et al., 2017; Wang et al., 2018). As long as the macroalgae stay on the very surface of water (as opposed to be

186   submerged under the surface), this assumption should be valid not just for macroalgae but for all floating matters.

187   Under high-wind conditions, the strong mixing may result in submerged algae (especially for microalgae), thus

188   violating the linear mixing rule. However, the cases presented in Figs. 2 - 5 were selected very carefully to avoid high

189   wind speed (> 5 m s^{-1}, where wind speed was obtained from the National Centers for Environmental Prediction).

190   Therefore, such mixing induced uncertainties are unlikely.

191   Additional uncertainties may come from the HICO radiometric calibration, which affects R_t and all derivative products.

192   Through the use of the Marine Optical Buoy (MOBY) and other clear-water sites, HICO has been calibrated

193   vicariously (Ibrahim et al., 2018), which resulted in significant improvements in the retrieved R_{rs} over water as

194   compared with data without vicarious calibration. However, after the vicarious calibration, while the spectral shape

195   of R_{rc} over water appears correct, the shape of ΔR_{rc} over land appears to be biased low at $\lambda > 800$ nm. Without vicarious

196   calibration, the opposite is observed. This is possibly due to the non-linear effects in the detector response to incoming

197   light, and currently there appears no reliable way to address this issue (A. Ibrahim, personal comm.). Similarly,

198   calibration for $\lambda < 450$ nm may be subject to larger errors than for λ between 450 and 800 nm. Therefore, R^{FM} in the

199   range of $800 - 900$ nm is omitted here, and interpretation of $400 - 450$ also requires more caution. Similarly, the

200   spectral wiggling between 700 and 800 nm (e.g., Fig. 3b) appears to come from residual errors in correcting water

201   vapor absorption and oxygen absorption in the atmosphere. Therefore, although the spectral wiggling does not affect

202   the overall shape of the red-edge reflectance, it may not be used for algorithm development to discriminate floating

203   matter types.

204   Indeed, with all these possible sources of uncertainties, such HICO-derived R^{FM} can still be used for spectral

205   discrimination of different floating matters without ambiguity, as shown below.

206   **4.2. Implications for spectral discrimination**

207   Spectral discrimination can be performed through either visual inspection or the use of certain type of similarity index

208   (e.g., SAM, Eq. 6). Here, results of the SAM analysis are presented in Table 1, followed by descriptions of visual

209   inspection to interpret the spectral similarity or difference. Because nearly all floating algae show typical red edge

210   reflectance (i.e., the sharp increase from about 670 nm to the NIR wavelengths), discrimination of different algae type

211   should focus on wavelengths < 670 nm. Furthermore, because HICO data are noisy for wavelengths < 450 nm, the

212   SAM calculation was restricted to $450 - 670$ nm from most R^{FM} spectra of Figs. $2 - 4$.

213   Table 1 shows the SAM results for three types of macroalgae (*Sargassum*, *Ulva*, kelp), three types of microalgae

214   (*Trichodesmium*, *Microcystic*, red *Nocticula scintillas* or *RNS*), and one type of organic matter (brine shrimp cysts or

215   *BSC*). For the same floating matter, if field-based R^{FM} is available, then it is used as the reference, otherwise the mean

216 HICO-derived R^{FM} is used as the reference. For SAM between different floating matters, all HCIO-derived R^{FM} from

217 both types are used (e.g., 4 *Sargassum* R^{FM} of Fig. 2a and 3 *Ulva* R^{FM} of Fig. 2b are used to calculate 12 SAM values),

218 with their mean and standard deviations listed in Table 1.

219

220 **Table 1. Spectral Angle Measure (degrees) between different floating matters for the spectral range of 450 – 670 nm, derived**

221 **from the HICO-derived and field-measured spectra shown in Figs. 2-4. An SAM of 0° indicates identical spectral shape,**

222 **while an SAM of 90° indicates completely different spectral shape. *Sarg*: *Sargassum fluitans/natans*; *Tricho*: *Trichodesmium*;**

223 ***Micro*: *Microcystis*; *RNS*: red *Noctiluca scintillas*; *BSC*: brine shrimp cysts.**

Sarg	**4.5±1.6**						
Ulva	27.2±2.5	**2.9±0.5**					
Kelp	13.7±1.8	32.5±1.3	**2.7±0.4**				
Tricho	15.4±4.6	25.1±2.0	23.1±3.2	**2.8±2.0**			
Micro	32.9±7.5	16.8±5.6	39.0±7.7	28.8±5.1	**4.6±2.5**		
RNS	9.9±2.4	31.4±2.8	16.7±3.0	17.2±2.1	34.7±6.7	**1.8±0.7**	
BSC	20.7±0.9	39.3±2.4	27.0±3.1	21.2±1.6	40.9±5.5	14.5±3.1	**1.1±0.0**
	Sarg	*Ulva*	*Kelp*	*Tricho*	*Micro*	*RNS*	*BSC*

224

225 For each type of floating matter, HICO-derived R^{FM} is very similar to either field-measured R^{FM} or to their mean R^{FM},

226 with SAM < 4.6°. In contrast, SAM between different floating matters is always > 9.9°, suggesting that all these

227 floating matters can be differentiated through spectroscopy analysis without any other ancillary information (e.g.,

228 knowledge of local oceanography or dominant floating algae type). This is despite the possible uncertainties in their

229 reflectance magnitude, as discussed above. Such an observation can also be explained through visual inspection.

230 From Fig. 2, it is clear that although the three types of macroalgae all share the same red-edge reflectance in the NIR,

231 they have different spectral shapes in the visible wavelengths. These characteristics make it easy to distinguish

232 *Sargassum* from *Ulva* (SAM > 27°, Table 1), as their reflectance peaks occur in different wavelengths in the visible.

233 For the same reason, it appears more difficult to spectrally discriminate *Sargassum* from kelp because they both have

234 reference peaks around 600 – 645 nm, and because they also share a common reflectance trough around 625 nm.

235 However, considering *Sargassum* is moving in the ocean while kelp is fixed in location, they can be separated using

236 sequential images. Even from a single image, when most visible wavelengths are used, *Sargassum* and kelp can still

237 be spectrally discriminated (SAM > 13°, Table 1). Within the group of *Sargassum* spectra (Fig. 2a), there is some

238 variability in the magnitude between 560 – 700 nm. It is unclear what caused such variability, although it could be

239 due to changes in carbon to chlorophyll ratio in *Sargassum* of different environment, as observed from kelp (Bell et

240 al., 2015). Such a variability, however, would not impact the spectral discrimination of *Sargassum* against other

241 floating matters, as SAM between *Sargassum* spectra is < 5°, much lower than between *Sargassum* and any other

242 floating matters (Table 1).

243 Similar to the macroalgae, the microalgae scums also show elevated NIR reflectance (Fig. 3), and their spectral shapes

244 in the visible make them straightforward to distinguish from each other (SAM > 17°), and also straightforward to

245 distinguish from macroalgae (SAM > 9.9°). One exception may be the cyanobacterial scums (blue-green algae blooms)

246 (Fig. 3b) as they show reflectance peak around 550 nm, similar to *Ulva* (Fig. 2b). However, reflectance around 550

247 nm is nearly symmetric for cyanobacterial scums, but asymmetric for *Ulva*. There is also a local reflectance trough

248 around 625 nm for cyanobacterial scums due to absorption of phycocyanin, but such a trough is lacking in the *Ulva*

249 spectra. Such characteristic makes it possible to differentiate between the two even without *a priori* knowledge of the

250 ocean or lake environment, as the SAM between the two groups is ~16.8° (Table 1). What's interesting is that within

251 each class, either *Trichodesmium* or *Microcystis*, although the spectral shape is nearly identical from different spectra

252 (SAM < 5°), there is substantial variability in the magnitude in the visible wavelengths, which might be due to changes

253 in their carbon to chlorophyll ratios (Behrenfeld et al., 2005). Furthermore, the spectral wiggling features between 450

254 and 660 nm in Fig. 3a are due to *Trichodesmium*-specific pigments. These features are unique to *Trichodesmium*

255 scums, which make it straightforward to develop classification algorithms once certain spectral bands are available to

256 capture these features.

257 Of all microalgae scums of Fig. 3, the spectral shapes of red *Noctiluca* (Fig. 3c) appear different from all others, but

258 they show the same characteristics as reported from the limited field measurements (Van Mol et al., 2007): a sharp,

259 featureless increase from ~520 nm to ~600 nm. This unique spectral shape makes *RNS* different from all other floating

260 matters (SAM > 9.9°, Table 1). The difference within this group is that the spectra from Sagami Bay off Japan show

261 reflectance troughs around 670 nm. Because red *Noctiluca* is known to feed on other algae, it is speculated that the

262 670-nm trough is due to chlorophyll pigments of the consumed algae. Once more hyperspectral data are available in

263 the future to test this hypothesis using field data, this characteristic may be used to study how red *Noctiluca* interacts

264 with other algae.

265 The non-algae floating matters in Fig. 4 show spectral characteristics different from both macroalgae and microalgae,

266 for example they lack the typical red-edge reflectance of vegetation, and lack of typical spectral variations in the

267 visible wavelengths due to pigment absorption. Within this group, the organic matters of BSC (Fig. 4a) and emulsified

268 oil (Fig. 4b) show some degrees of similarity as they also have monotonic reflectance increases from a wavelength

269 between 500 – 560 nm to at least 740 nm. The difference between them is that BSC reflectance starts to increase

270 always at ~560 nm with an inflection wavelength ~640 nm, while reflectance of oil emulsions start to increase at

271 variable wavelengths without any inflection between 560 – 740 nm. Indeed, the infection at ~640 nm appears to be a

272 common feature between BSC slicks and coral spawn slicks (Yamano et al., 2020). In contrast, depending on the oil

273 emulsion state, oil emulsion may have different spectral characteristics (Lu et al., 2019), suggesting that there is no

274 fixed "endmember" spectra for oil spills.

275 The inorganic "particles" (i.e., water bubbles, ice) also have distinctive spectral shapes. The examples in Fig. 4c

276 indicate that submersed bubbles from shipwakes are similar in spectral shapes, but all others are nearly identical in

277   their lack of any spectral features. Rather, foams, whitecaps, and ice all show flat reflectance spectral shapes between

278   400 – 800 nm that are consistent with *in situ* measurements of foams (Dierssen, 2019). The lack of spectral features

279   is similar to marine debris (Garaba and Dierssen, 2020). Such a similarity will make detection of marine debris very

280   difficult, especially around ocean fronts because these are where surface materials tend to aggregate and foams also

281   tend to form.

282   In addition to the spectra of Figs. 2-4 that can be well recognized, HICO also showed reflectance spectra that are

283   difficult to discriminate from pure spectroscopy, as shown in Fig. 5. Without a known reflectance library, one can

284   only speculate what algae type could be responsible for the algae scum spectra from some ancillary information in the

285   literature. For example, the often reported blooms of *Lingulodinium polyedrum* and *Akashiwo sanguinea* in coastal

286   waters off southern California and in Monterey Bay, respectively, may show spectral shapes of Fig. 5a when they are

287   heavily concentrated in surface waters. Inference may also be made for other cases once similar ancillary information

288   is available. Even when such information is absent, one can still rule out some possibilities simply based on the spectral

289   shapes. For example, the reflectance spectrum in Fig. 5b from Lake Victoria cannot be from cyanobacteria that has

290   been often reported in this lake (Fig. 3b), but it is most likely from a dinoflagellate bloom, as blooms of other algae

291   types have also been reported in this lake (Haande et al., 2011). Likewise, the different spectra from the same Taganrog

292   Bay in Figs. 5c & 5d suggest different algae type. Clearly, although cyanobacterial blooms have been reported in

293   many lakes, without spectral diagnosis one cannot simply jump to the conclusion that a freshwater bloom is caused

294   by a certain type of cyanobacterium.

295   **4.3. Implications for current and future satellite missions**

296   Because HICO is a pathfinder sensor that collected only a limited number of scenes, not all reported floating matters

297   have been captured. For example, no HICO scene appears to have captured pumice rafts, *Sargassum horneri*, or marine

298   debris. Therefore, the spectral reflectance dataset presented here is incomplete. The use of data from other similar

299   pathfinders, for example the DLR Earth Sensing Imaging Spectrometer (DESIS) on the ISS (235 bands from 400 –

300   1000 nm, 30-m resolution, 2008 – present), may complement the spectral data using the same approach. Even at its

301   present form, given the large variety of floating matters presented here, the spectral data may lead to several

302   implications for current and future satellite missions.

303   First, although all current multi-band sensors can detect floating matters through their elevated NIR reflectance (Qi et

304   al., 2020), the Sentinel-3 Ocean and Land Colour Imager (OLCI) appears to be the best to differentiate spectral shapes

305   in the visible wavelengths because of its 21 spectral bands between 400 and 1,020 nm, especially because of its 620-

306   nm that can be used to differentiate whether an algae scum appears greenish or brownish, thus providing extra

307   information to discriminate algae type in the absence of hyperspectral data.

308   Second, for the same reason, if there is room to allow for more than 4 bands such as those on the PlanetScope (DOVE)

309   constellations, a 5th band may be placed around 620 nm. Then, with the existing bands in the blue, green, red, and NIR

310   region, such a 5-band sensor may significantly enhance the capacity of the current high-resolution (~ 3-4 m), 4-band

311   sensors in differentiating greenish and brownish algae types.

312   Finally, the Ocean Color Instrument (OCI) on NASA's PACE mission, to be launched in 2023, will be the first of its
313   kind to map global oceans with hyperspectral capacity (5 nm resolution between 340 – 890 nm, plus 7 discrete bands
314   from 940 to 2260 nm) with a nominal resolution of 1 km. Unlike HICO, OCI will cover global oceans and lakes every
315   1-2 days, thus providing unprecedented opportunities to detect, differentiate, and quantify various types of floating
316   matters. The spectral reflectance data, derived from one sensor (HICO) with a stable calibration, may serve as a
317   consistent dataset to help select the optimal bands towards future applications once PACE data becomes available, for
318   example, through the use of SAM matrix as demonstrated in Table 1. Likewise, the SBG mission currently being
319   planned by NASA is expected to have hyperspectral capacity between 380 and 2500 nm with a nominal resolution of
320   30 m (Cawse-Nicholson et al., 2021); such a mission will provide unprecedented opportunity to map various floating
321   matters on a global scale where the hyperspectral dataset developed here can help develop algorithms before its launch.

322   **5. Conclusion**

323   Through customized atmospheric correction and spectral unmixing, hyperspectral reflectance in the visible and NIR
324   wavelengths of various floating matters have been derived from HICO measurements over global oceans and lakes.
325   The reflectance dataset shows distinguishable spectral shapes between floating algae (macroalgae and microalgae)
326   and non-algae floating matters, and also distinguishable spectral shapes in the visible wavelengths between different
327   floating algae types. While the approach may be extended to other pathfinder missions to complement the findings
328   here, the spectral reflectance dataset is expected to help select optimal bands for future hyperspectral satellite missions
329   to differentiate and quantify the various floating matters in global oceans and lakes.

330   **Data Availability**

331   All HICO data used in this analysis are available at the NASA Ocean Biology Distributed Active Archive Center
332   (OB.DAAC, https://oceancolor.gsfc.nasa.gov). The data processing software (SeaDAS) can be obtained from the same
333   source, at https://seadas.gsfc.nasa.gov. The derived HICO spectra in digital data form, as shown in the above figures,
334   are available on-line from the Ecological Spectral Information System (EcoSIS) (http://ecosis.org, doi:
335   10.21232/74LvC3Kr) (Hu, 2021b).

340 **References**

341 [1] Behrenfeld, M. J., E. Boss, D. A. Siegel, and D. M. Shea (2005). Carbon-based ocean productivity and
342   phytoplankton physiology from space. Global Biogeochemical Cycles, 19, GB1006,
343   doi:10.1029/2004GB002299.

344 [2] Bell, T. W., K. C. Cavanaugh, and D. A. Siegel (2015). Remote monitoring of giant kelp biomass and
345   physiological condition: An evaluation of the potential for the Hyperspectral Infrared Imager (HyspIRI)
346   mission. *Remote Sens. Environ.*, 167:218-228.

347 [3] Casey, K. A., C. S. Rousseaux, W. W. Gregg, et al. (2020). A global compilation of in situ aquatic high
348   spectral resolution inherent and apparent optical property data for remote sensing applications. Earth Syst. Sci.
349   Data, 12:1123-1139. https://doi.org/10.5194/essd-12-1123-2020.

350 [4] Cawse-Nicholson, K. P. A. Townsend, D. Schimel, et al. (2021). NASA's surface biology and geology
351   designated observable: A perspective on surface imaging algorithms. *Remote Sens. Environ.*, 257, 112349,
352   https://doi.org/10.1016/j.rse.2021.112349

353 [5] Dierssen, H. (2019). Hyperspectral Measurements, Parameterizations, and Atmospheric Correction of
354   Whitecaps and Foam From Visible to Shortwave Infrared for Ocean Color Remote Sensing. Front. Earth Sci.
355   7:14. doi: 10.3389/feart.2019.00014.

356 [6] Garaba, S. P., and H. M. Dierssen (2018). An airborne remote sensing case study of synthetic hydrocarbon
357   detection using short-wave infrared absorption features identified from marine-harvested macro- and
358   microplastics. *Remote Sens. Environ.* 2018, *205*, 224–235.

359 [7] Garaba, S. P., and H. M. Dierssen (2020). Hyperspectral ultraviolet to shortwave infrared characteristics of
360   marine-harvested, washed-ashore and virgin plastics. Earth Syst. Sci. Data, 12, 77–86, 2020
361   https://doi.org/10.5194/essd-12-77-2020.

362 [8] Gower, J., Hu, C., Borstad, G., King, S. (2006). Ocean color satellites show extensive lines of floating
363   Sargassum in the Gulf of Mexico. *IEEE Transactions on Geoscience and Remote Sensing*, 44, 3619-3625.

364 [9] Haande, S., Rohrlack, T., Semyalo, R.P., Brettum, P., Edvardsen, B., Lyche-Solheim, A., Sørensen, K., &
365   Larsson, P. (2011). Phytoplankton dynamics and cyanobacterial dominance in Murchison Bay of Lake Victoria
366   (Uganda) in relation to environmental conditions. *Limnologica-Ecology Management of Inland Waters, 41*, 20-
367   29.

368 [10] Hu, C., Carder, K. L., and Muller-Karger, F. E. (2000), Atmospheric correction of SeaWiFS imagery over
369   turbid coastal waters: a practical method, Remote Sens. Environ. 74:195-206.

370 [11] Hu, C., L. Feng, Z. Lee, C. O. Davis, A. Mannino, C. R. McClain, and B. A. Franz (2012). Dynamic range and
371   sensitivity requirements of satellite ocean color sensors: learning from the past. Appl. Opt., 51:6045-6062.

372 [12] Hu, L., Hu, C., & Ming-Xia, H. (2017). Remote estimation of biomass of Ulva prolifera macroalgae in the
373   Yellow Sea. *Remote Sensing of Environment, 192*, 217-227.

374 [13] Hu, C. (2021a). Remote detection of marine debris using satellite observations in the visible and near infrared
375   spectral range: Challenges and potentials. *Remote Sens. Environ*., 259,
376   112414, https://doi.org/10.1016/j.rse.2021.112414

377   [14] Hu, C. (2021b). Floating matter reflectance from HICO. Data set. Available on-line [http://ecosis.org] from the
378   Ecological Spectral Information System (EcoSIS). 10.21232/74LvC3Kr.
379   [15] Ibrahim, A., B. A. Franz, Z. Ahmad, R. Healy, K. Knobelspiesse, B-C. Gao, C. Proctor, and P-W. Zhai (2018).
380   Atmospheric correction for hyperspectral ocean color retrieval with application to the Hyperspectral Imager
381   for the Coastal Ocean (HICO). *Remote Sensing of Environment*, 204:60-75,
382   http://dx.doi.org/10.1016/j.rse.2017.10.041.
383   [16] IOCCG (2014). Phytoplankton Functional Types from Space. Sathyendranath, S. (ed.), Reports of the
384   International Ocean-Colour Coordinating Group, No. 15, IOCCG, Dartmouth, Canada.
385   [17] Kruse, F, A., A.B. Lefkoff, J.W. Boardman, K.B. Heidebrecht, A.T. Shapiro, P.J. Barloon, A.F.H. Goetz
386   (1993). The spectral image processing system (SIPS)—interactive visualization and analysis of imaging
387   spectrometer data. *Remote Sensing Environ.*, 44:145-163.
388   [18] Lu, Y., Shi, J., Wen, Y., Hu, C., Zhou, Y., Sun, S., Zhang, M., Mao, Z., & Liu, Y. (2019). Optical
389   interpretation of oil emulsions in the ocean – Part I: Laboratory measurements and proof-of-concept with
390   AVIRIS observations. *Remote Sensing of Environment, 230*, 111183.
391   https://doi.org/10.1016/j.rse.2019.05.002.
392   [19] McKinna, L.I.W. (2015). Three decades of ocean-color remote-sensing Trichodesmium spp. in the World's
393   oceans: A review. *Progress in Oceanography, 131*, 177-199.
394   [20] Qi, L., C. Hu, K. MIkelsons, M. Wang, V. Lance, S. Sun, B. B. Barnes, J. Zhao, and D. V. der Zande (2020).
395   In search of floating algae and other organisms in global oceans and lakes. Remote Sens. Environ., 239,
396   111659, https://doi.org/10.1016/j.rse.2020.111659.
397   [21] Van Mol, B., Ruddick, K., Astoreca, R., Park, Y., & Nechad, B. (2007). Optical detection of a Noctiluca
398   scintillans bloom. *EARSeL eProceedings, 6*, 130-137.
399   [22] Wang, M., Hu, C., Cannizzaro, J., English, D., Han, X., Naar, D., et al. (2018). Remote sensing of Sargassum
400   biomass, nutrients, and pigments. Geophysical Research Letters, 45.https://doi.org/10.1029/2018GL078858
401   [23] Yamano, H., A. Sakuma, and S. Harii (2020). Coral-spawn slicks: Reflectance spectra and detection using
402   optical satellite data. Remote Sens. Environ., 251, https://doi.org/10.1016/j.rse.2020.112058.
403